ADAPTIVE SEGMENTATION OF CELLS AND PARTICLES IN FLUORESCENT MICROSCOPE IMAGES

Birgit Möller, Oliver Greß
Institute of Computer Science, Martin-Luther-University Halle-Wittenberg
Von-Seckendorff-Platz 1, 06099 Halle/Saale, Germany

Nadine Stöhr, Stefan Hüttelmaier
ZAMED, Martin Luther University Halle-Wittenberg

Stefan Posch
Institute of Computer Science, Martin Luther University Halle-Wittenberg

Keywords: Active contours, Snakes, Wavelets, Segmentation, Fluorescent microscope images.

Abstract: Microscope imaging is an indispensable tool in modern systems biology. In combination with fully automatic image analysis it allows for valuable insights into biological processes on the sub-cellular level and fosters understanding of biological systems. In this paper we present two new techniques for automatic segmentation of cell areas and included sub-cellular particles. A new cascaded and intensity-adaptive segmentation scheme based on coupled active contours is used to segment cell areas. Structures on the sub-cellular level, i.e. stress granules and processing bodies, are detected applying a scale-adaptive wavelet-based detection technique. Combining these results allows for complementary analysis of biological processes. It yields new insights into interactions between different particles and distributions of particles among different cells. Our experimental evaluations based on ground-truth data prove the high-quality of our segmentation results regarding these aims and open perspectives towards deeper insights into biological systems on the sub-cellular level.

1 INTRODUCTION

Advances in fluorescence microscopy imaging allow to study processes at a cellular level and supply a valuable source of information for modern systems biology. One of the questions which can be approached by this technique is the analysis of different sub-cellular particles in eucaryotic cells which are amongst others thought to be places of distinct functions. Two kinds of such sub-cellular particles are processing bodies (PBs) and stress granules (SGs), see Figure 1 for example image clips.

PBs are suggested to be places of mRNA degradation in eucaryotic cells as enzymes of the degradation machinery are enriched in these foci (Eulalio et al., 2007). However, if this function indeed can be referred to the particles remains elusive. The second class of foci are SGs emerging during cellular stress conditions (Yamasaki and Anderson, 2008). SGs are assumed to be essential for mRNA storage during stress (Yamasaki and Anderson, 2008), although this presumption needs to be validated as well. To study if or to what extent visible SGs and PBs can be connected to a function within the cell it is essential to monitor their occurrence. It is particularly of interest in which cells of a given cell population the particles appear and if and how they interact with each other. Also their distribution *inside* the different cells yields valuable information for biological investigations. To answer these questions the need arises to not only automatically detect PBs and SGs in microscope images, but also to segment complete cell areas.

In biomedical experiments sub-cellular particles of interest are fluorescently labeled in different chromatographic bands yielding multi-channel images which are subsequently analyzed by automatic image

Möller B., Greß O., Stöhr N., Hüttelmaier S. and Posch S. (2010).
ADAPTIVE SEGMENTATION OF CELLS AND PARTICLES IN FLUORESCENT MICROSCOPE IMAGES.
In *Proceedings of the International Conference on Computer Vision Theory and Applications*, pages 97-106
DOI: 10.5220/0002849100970106

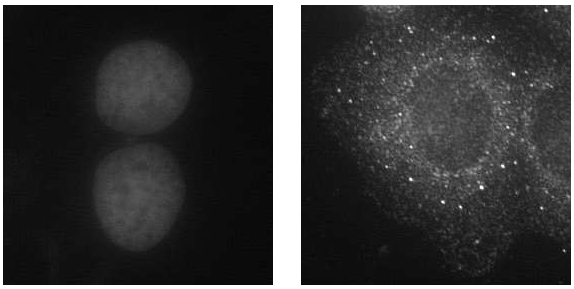

(a) (b)

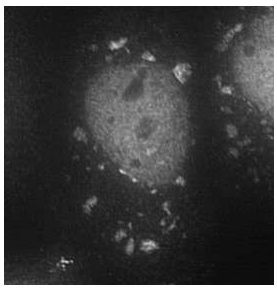

(c)

Figure 1: Fluorescently labeled nuclei and sub-cellular particles: (a) two cell nuclei, (b) a cell with labeled PBs, and (c) one with labeled SGs.

analysis techniques. Unfortunately explicit labeling of the complete cell area is typically not possible and enforces to extract it from one of the available channels originally intended for detection of other particles. In our experimental data each image contains three channels. In the nucleus channel of the images nuclei manifest themselves by more or less homogeneously textured bright blobs. PBs are small bright spots with a quite small variance in size while SGs are usually significantly larger than PBs and show a large variance in size (cf. Fig. 1).

Due to the significant variation in appearance of the different sub-cellular particles there is no integrated segmentation approach that allows to detect all kinds of particles and the cells themselves. Accordingly, we apply two different techniques for detecting PBs and SGs on the one hand, and the cell areas on the other. PBs and SGs detection relies on a scale-adaptive wavelet-based detection approach able to cope with the variance in size of these particles (Greß et al., 2010). Cell area segmentation is conducted in the fluorescence channel for PBs in each image. To solve the task we adopt coupled active contour models.

One main contribution of this paper is the scale-adaptive extension of a wavelet-based particle detection algorithm. As the second main contribution we present an extension of active contour models towards a new cascaded segmentation scheme that yields larger flexibility in segmenting objects with specific intensity distributions. In detail, since the target area of a cell does not show significant discontinuities along its border and also cannot be modeled by one homogeneous intensity distribution, customary active contour energy models are not appropriate to solve the given task. Our new cascaded approach overcomes these problems and allows to cope with objects of non-homogeneous intensity distributions and weak discontinuities along their borders by incremental adaptation to the objects' intensity characteristics.

The remainder of this paper is organized as follows. After reviewing related work in the next section, we introduce our scale-adaptive wavelet-based approach to particle detection in Section 3. In Section 4 the new cascaded technique for intensity-adaptive cell segmentation is presented. Subsequently experimental evaluations based on ground-truth data are discussed (Section 5), and we conclude with some final remarks in Section 6.

2 RELATED WORK

Segmentation of cells and detection of particles in fluorescently labeled microscopy images are instances of general problems in image analysis. Due to the special characteristics of these images, adaptations are required and have been proposed.

In (Dzyubachyk et al., 2007) and (Dzyubachyk et al., 2008) a level-set based approach for segmentation and tracking of cells is proposed. For initial segmentation in the first time frame, the fitting term of the classical Chan-Vese model (Chan and Vese, 2001) is replaced with a Gaussian likelihood for the intensity values with unknown variance. Lumped cells are separated using the watershed transform and subsequent region merging. For tracking a multi phase level-set technique is used employing a coupling term of multiple level-set functions as proposed in (Dufour et al., 2005). Approaching cells are separated via the Radon-Transform in addition to the coupling term.

Several approaches exist for the detection of spot-like particles, e.g. still using global and local thresholding techniques like Otsu's global method or the local Niblack operator (Xavier et al., 2001; Bolte and Cordelieres, 2006). Further techniques include sampling from an image intensity density estimated via h-dome transform and subsequent clustering of samples (Smal et al., 2008). The method in (Olivo-Marin, 2002; Genovesio et al., 2006) is based on wavelet decomposition, but best-suited to detect particles with

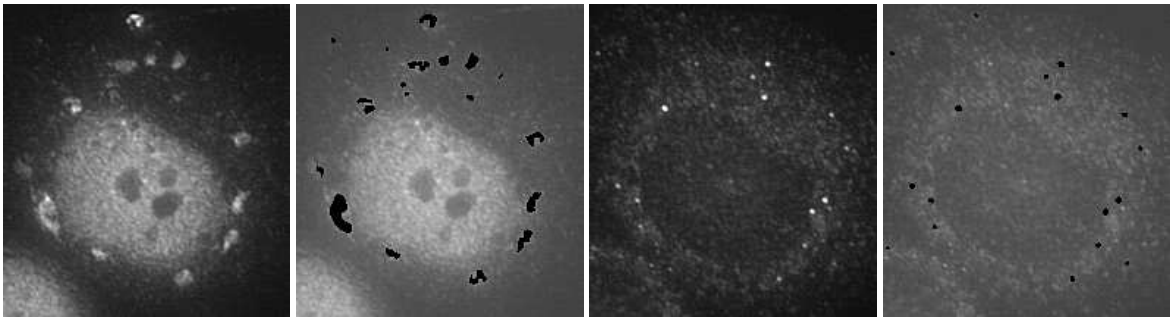

(a) (b) (c) (d)

Figure 2: Examples of fluorescently labeled particles. (a) SG channel. (b) Detected SGs (black) using the scale-adaptive wavelet algorithm. (c) PB channel. (d) Detected PBs (black) using the same algorithm. Image intensity values in (b) and (d) are scaled for better visualization of detected particles.

limited variation in size.

An integrated algorithm for cell area segmentation and sub-cellular particle detection was proposed by (Dufour et al., 2008). They combine wavelet-based particle detection adopting the approach of (Olivo-Marin, 2002) with active contour-based cell area segmentation. Unfortunately their snake energy is not transferable to our domain as the cells in our scenario show quite inhomogeneous and grainy intensity distributions which do not allow for easy modeling within a snake energy functional.

3 DETECTION OF PARTICLES

To detect particles in microscopy images we recently proposed (Greß et al., 2010) to extend the method of (Olivo-Marin, 2002; Genovesio et al., 2006), because more flexibility with regard to size of particles to be detected is required by the nature of stress granules.

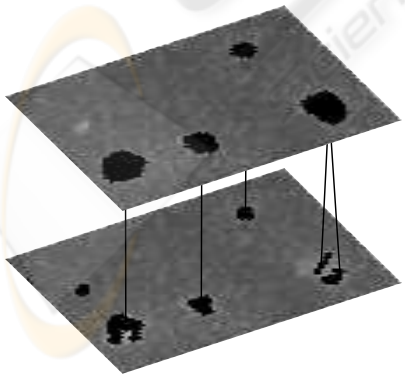

Figure 3: Hypotheses trees for a clip of two correlation images.

Detection as suggested in (Olivo-Marin, 2002) uses the *a trous* wavelet transform on basis of third order B-spline wavelets yielding wavelet coefficients

$$W_s(x,y) = I_s(x,y) - I_{s-1}(x,y), \quad s \in \{1,\dots S\}, \quad (1)$$

where s denotes the scale and $I_1(x,y),\dots,I_S(x,y)$ are recursively smoothed versions of the original input image $I_0(x,y)$.

Denoised wavelet coefficients $\tilde{W}_s(x,y)$ are obtained applying the amplitude-scale-invariant Bayes estimator (Figueiredo and Nowak, 2001). Wavelet coefficients of adjacent scales are highly correlated across scales due to the nature of the wavelet transform applied, which motivates the combination of adjacent scales $s \in [a,b]$ to *correlation images*

$$c_{[a,b]}(x,y) = \prod_{s=a}^{b} \tilde{W}_s(x,y). \quad (2)$$

Regions with large values in the correlation image are assumed to correspond to particles, thus, finding connected components after global thresholding yields the detection result.

Particles of a certain size are best represented in a particular interval of scales, therefore one interval is appropriate if all particles in the image share similar size characteristics. However, if a single scale interval does not properly match the characteristics of the particles to be detected, irrelevant scales are included or important ones are excluded, causing incorrect sizes or shapes in detection, or leading to complete loss of particles.

The use of multiple correlation images of – usually overlapping – scale intervals $[a_n,b_n]$ allows the detection of a particle in the scale interval which best suits its characteristics. However, in many cases the particle is also found in adjacent intervals with incorrect size or shape. This causes spatially overlapping and thus competing particle hypotheses from different scale intervals, from which we need to select the correct one. Overlapping and thus competing hypotheses are organized in a tree with leaves corresponding

to the finest scale interval where hypotheses are available. Coarser scale hypotheses appear closer to the root, as illustrated in Fig. 3.

The concept of meaningful events (Desolneux et al., 2003) is employed to delete nodes of inferior hypotheses from the tree. This meaningfulness can be understood as the significance of an event produced by a background process or under a null hypothesis respectively, and has strong relation to statistical hypothesis testing. The background process H_0 employed in our model assumes that no particle exists at the present location and correlation image values are caused by noise. Correlation values are supposed to be pairwise independent, which allows us to represent the probability $P(F_i \mid H_0)$ that particle F_i is produced by the background process H_0 as

$$P(F_i \mid H_0) = \prod_{(x,y)\in F_i} P\left(C_{[a_n,b_n]}(x,y) = c_{[a_n,b_n]}(x,y) \mid H_0\right),$$

where $C_{[a_n,b_n]}(x,y)$ are random variables modeling the correlation value for interval $[a_n,b_n]$ observed at pixel position (x,y). We denote with $p(F_i)$ the p-value of F_i, which is the probability to observe correlation values *at least as extreme* as the values of F_i produced by H_0:

$$p(F_i) = \prod_{(x,y)\in F_i} P\left(C_{[a_n,b_n]}(x,y) \geq c_{[a_n,b_n]}(x,y) \mid H_0\right).$$

The tree of competing hypotheses is reduced comparing p-values. To account for the difference in size of the support of hypotheses, the p-value of a node is normalized by the size of its support. Starting from the leaves, a parent's normalized p-value is compared to the product of the normalized p-values of its children. Hypotheses with smaller p-values are kept as they are assumed to be more unlikely caused by noise.

The described method is able to select detection candidates from the correct scale interval. Examplary detection results for SGs and PBs are shown in Fig. 2 where SGs are hypothesized in intervals $[2,3]$ and $[3,4]$ and selected from the appropriate interval according to their size.

4 CELL SEGMENTATION

4.1 Snake Basics

Active contours can either be modeled implicitly adopting level-set approaches or explicitly in terms of parametric contour models, i.e. snakes. While the numerical tractability of level-set approaches is often superior compared to snake optimization techniques, topology preservation is usually easier to guarantee by snake approaches as topological stability is inherent in the model theory underlying snakes. In our scenario the number of objects to segment is known in advance, hence the topology of the desired segmentation result is known. For this reason we prefer explicit active contour models for this application.

In explicit approaches the contour of an object is defined as a function $c : R \rightarrow R^2$ which maps a parameter value $s \in [0,1]$ defined along a given contour c to points (x,y) in 2-D space. For object segmentation an energy functional over the contour function $c(s)$ is defined. The contour is evolved towards a local minimum of the energy, which gives the final segmentation result.

In general the energy functional of an explicit active contour consists of two types of energy terms. On the one hand we have an internal energy term $E_{int}(c(s))$ solely depending on the contour itself, e.g. its length and curvature,

$$E_{int}(c(s)) = \frac{1}{2}\int_0^1 \alpha \cdot \| c'(s) \|^2 + \beta \cdot \| c''(s) \|^2 \, ds, \quad (3)$$

where α and β are weighting constants. On the other hand we have an external energy term which is usually derived from the input image to be segmented,

$$E_{ext}(c(s)) = \int_0^1 f_{ext}(c(s))ds. \quad (4)$$

During segmentation the snake is iteratively moved to minimize the composed snake energy

$$E(c(s)) = E_{int}(c(s)) + E_{ext}(c(s)). \quad (5)$$

The optimization procedure relies on implicit gradient descent techniques, introducing a time t to model the contour evolution process, and given Euler-Lagrange formulations (Kass et al., 1988) of the snake energy functional:

$$c_t(s) = c_{t-1}(s) - \frac{1}{\gamma} \cdot \frac{dE(c_t(s))}{dc_t(s)}. \quad (6)$$

γ denotes the step-size for the gradient descent step in each iteration.

4.2 Region Homogeneity Criterium

In contrast to several related papers on cell segmentation for fluorescent microscope images our target objects, i.e. the cell areas, are not characterized by significant gray-scale discontinuities along their boundaries. Rather they show specific region intensity profiles (cf. Fig. 4 (a)). Accordingly, widely used external snakes energies like gradient-based terms do not provide helpful information for our application. We therefor replace E_{ext} as defined in Eq. 4 by a snake energy term proposed in (Chan and Vese, 2001) which

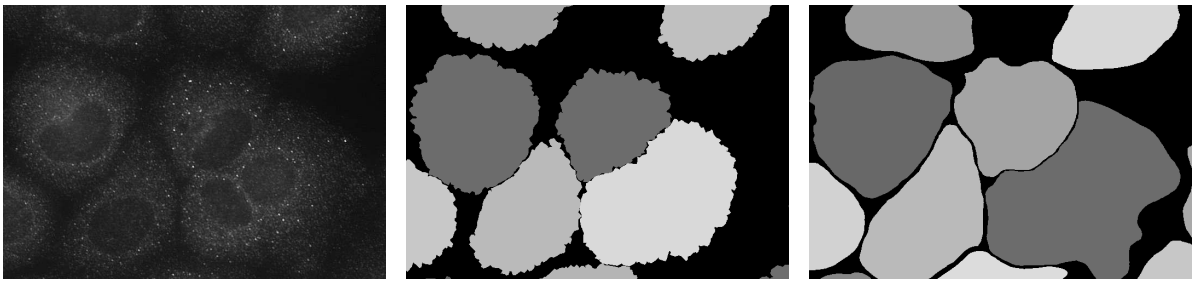

(a) (b) (c)

Figure 4: Example image clip showing (a) dark nuclei surrounded by cell area and fluorescently labeled PBs, (b) the mask corresponding to the automatic segmentation result, and (c) the manually labeled ground-truth mask for comparison.

considers not only image intensity information along the snake itself but also intensity data of the complete image domain Ω. In particular, the intensities for the interior and exterior regions of the snake, $R_{in}(c(s))$ and $R_{out}(c(s))$ respectively, are modeled as constant and are denoted by c_{in} and c_{out}. Deviations from these constant intensities are penalized as follows:

$$E_r(c(s)) = \lambda_{in} \cdot \int_{R_{in}(c(s))} (I(x,y) - c_{in})^2 \, d\Omega + \lambda_{out} \cdot \int_{R_{out}(c(s))} (I(x,y) - c_{out})^2 \, d\Omega, \quad (7)$$

where $I(x,y)$ is the input image intensity at pixel position (x,y) and λ_{in} and λ_{out} are weighting constants. During optimization this term pushes the snake to a location where its interior pixel value distribution is well described by c_{in}, and the remaining exterior pixel value distribution by c_{out}. It is noted that this model of constant intensities and quadratic error terms is approximately equivalent to a Gaussian model with means c_{in} and c_{out} and standard deviations λ_{in} and λ_{out}, see e.g. (Dzyubachyk et al., 2007).

4.3 Snake Coupling

The typical use case of snake-based segmentation assumes a single snake to be optimized within a given image at a single point in time. For our application, however, we aim at segmenting a set of multiple cells. In particular, information about the contour of one cell directly effects the contour of neighboring cells. Most importantly it has to be ensured that snakes do not overlap which would correspond to overlapping cells that do not occur in reality. Consequently, proper segmentation of the complete image is only possible by performing an integrated optimization of all cell contours in parallel. We adopt the approach of (Zimmer and Olivo-Marin, 2005) and introduce a common energy functional E_c for N snakes including internal snake energies (Eq. 3), region homogeneity criteria (cf. Eq. 7) and an energy term that allows to penalize overlapping snake regions:

$$\begin{aligned} E_c(c_1(s),\ldots,c_N(s)) &= \sum_{i=1}^{N} E_{int}(c_i(s)) \\ &+ \lambda_{in} \cdot \sum_{i=1}^{N} \int_{R_{in}(c_i(s))} \left(I(x,y) - c_{in}^i\right)^2 d\Omega \\ &+ \lambda_{out} \cdot \int_{\Omega \setminus (\bigcup_{i=1}^{N} R_{in}(c_i(s)))} (I(x,y) - c_{out})^2 \, d\Omega \\ &+ \rho \cdot \sum_{i=1}^{N} \sum_{j=i+1}^{N} \int_{R_{in}(c_i(s)) \cap R_{in}(c_j(s))} 1 \, d\Omega \ . \end{aligned} \quad (8)$$

The last summand considers for each pair of snakes $(c_i(s), c_j(s))$ the area of interior overlap $R_{in}(c_i(s)) \cap R_{in}(c_j(s))$ and weights it with a constant ρ.

For optimization the Euler-Lagrange functional with regard to each single snake $c_i(s)$ is derived yielding N evolution equations in total. These are individually optimized following the implicit approach proposed in Eq. 6.

4.4 Cascaded Active Contours

Analyzing the general appearance of cells in our application it becomes obvious that their region intensity distribution cannot very well be modeled by a Gaussian intensity distribution underlying E_r in Eq. 7. Rather several rings of approximately Gaussian intensity value distributions can be identified enclosing the central nucleus region of a cell (cf. Fig. 4 (a)). The average intensities of these rings monotonically decrease from the nucleus region towards the outer sections of the cell.

Due to this intensity distribution of cells the above model is not very well suited to segmented a complete cell. One option is to adapt the intensity model for cell regions according to intensity profiles observed. However, this is quite difficult as not only more sophisticated intensity distributions like Gaussian mixtures need to be integrated, but also the characteristic

spatial variations of the intensity values require proper consideration.

As an alternative we apply a cascaded segmentation approach. For initialization we detect nucleus regions and use their contours as initial snakes for the cells. The segmentation process consists of three subsequent levels of snake optimization. Each level aims at extending the current segmentation result towards the next outward intensity ring of the cell.

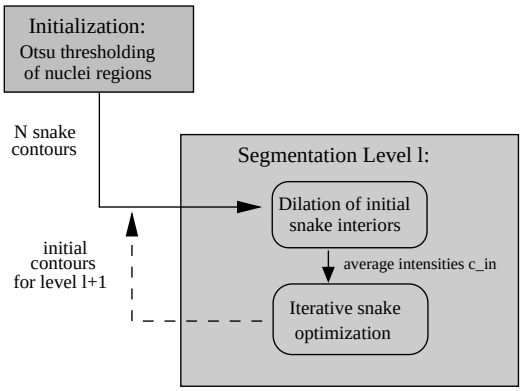

Figure 5: Overview of the cascaded segmentation approach.

Fig. 5 shows a diagram of the cascaded segmentation algorithm with its three levels. The initial nucleus segmentation is accomplished using a global Otsu's thresholding followed by morphological closing. For each connected component a cell is hypothesized and its contour yields an initial snake.

At the beginning of each segmentation level l the interior of each initial snake contour for this level is dilated by 10 pixels. This dilation is constraint to avoid overlap between neighboring snakes. From each expanded image region of approximately 10 pixel width the average intensity is extracted for snake $c_n(s)$ and used as initial constant $c_{in}^{l,n}$ for the subsequent optimization level.

As this initial average intensity tends to be smaller than $c_{in}^{l-1,n}$ extracted during the previous segmentation level, the snake is driven to evolve towards the outside for integrating the new darker regions into the cell. Each snake finally converges to a position where its overall energy is minimized according to Eq. 8. This result is subsequently used as contour initialization in the subsequent segmentation level. In conclusion, each snake incrementally includes darker regions into its area, and finally stops at the border to the background of the outmost lying intensity ring.

5 RESULTS

In the following we discuss experimental results of our cascaded segmentation approach. In particular, we will show the high quality of the cell segmentation by comparing our results to manually labeled ground-truth data. For PBs and SGs the assignment to individual cells is assessed given automatic and ground-truth cell segmentation.

5.1 Image Data

The algorithm was evaluated on 5 sample images resulting from a common experimental setup. The cells stem from the human hepatoma cell line (HUH7 cells). Each image consists of three channels, containing fluorescently labeled nuclei, SGs and, PBs respectively. SGs are labeled by immunostaining of TIAR (a protein localized in SGs), while PBs are labeled by immunostaining of DCP1a (decapping enzyme localized in PBs). The nuclei are labeled by DAPI.

In total, all images include 86 cells manually labeled for ground-truth. Initial snakes for the snake segmentation are derived from detected cell nuclei as explained above. It may happen during nuclei detection that nuclei located very close to each other are fused into a single nucleus region. In such cases snakes are missing, i.e. not all ground-truth cells can properly be segmented with the given set of initial snakes. To nevertheless enable a fair evaluation of the snake segmentation approach and due to the fact that the automatic nucleus detection algorithm is not part of this contribution, the labeling of ground-truth cells was adapted accordingly for such cells. In detail, if two or three nuclei merged during automatic segmentation also the cells involved were merged in manual ground-truth labeling. After adaptation 77 ground-truth cells remain for evaluation.

5.2 Segmentation Results

The cascaded segmentation algorithm was applied with three levels, each with its own parameter settings (Tab. 1). Note that for all images and each of the three levels the same set of parameters was applied.

When optimizing snakes in practice one important issue to ensure accurate and comparable localization properties at each point position along the contour is to keep the distance between subsequent points of the snake, i.e. the length of the snake segments, more or less uniform. In our approach the snake is parameterized with the desired segment length l_{seg}, and every second iteration the segments are checked and in case

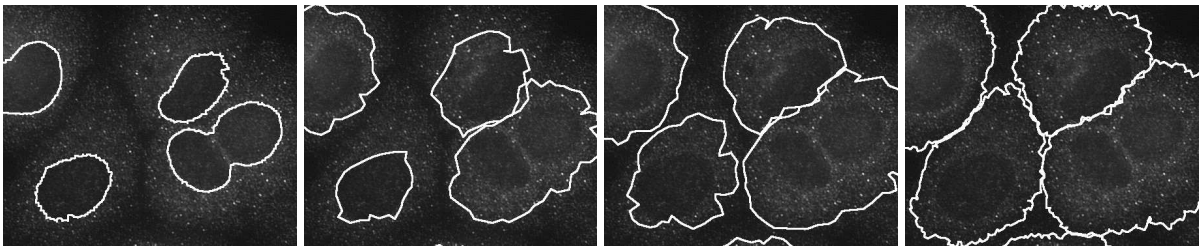

(a) (b) (c) (d)

Figure 6: Cropped image section showing the evolution of the snake starting with the initial snakes extracted from the nucleus regions (a) and the results of subsequent optimization levels 1 to 3 (b-d).

of large deviations from the optimum segment length points are added or deleted accordingly.

The snake is supposed to stop in a locally optimal energy state, i.e. a position of minimal snake energy. In our setup we use a combination of two stopping criteria for checking if the snake converged. On the one hand we analyze the relative change in the area of snake interior between two iterations and stop optimization if it falls below a certain threshold value ΔA. In addition, a maximum number of admissible iterations I_{max} is defined mainly to prevent the snake from oscillating between two steady states with difference in area size just below the threshold ΔA.

In general, during the first two levels the overall shape of the cells is extracted. In level 3 accurate local segmentation and local improvements with regard to low intensity regions get higher priority. Accordingly the weight of the curvature term is increased, the length of the contour segments is decreased and the stopping criteria are adapted.

Table 1: Parameters used during snake segmentation.

Level:	1st	2nd	3rd
λ_{in}	0.1		
λ_{out}	25		
ρ	10000		
α	1.25		
β	0.75		1.25
γ	0.0001		0.0002
l_{seg}	15		5
ΔA	0.015	0.005	0.001
I_{max}	100		200

Prototypical segmentation results of our approach are shown in Figs. 4, 6 (d), and 7. Comparing the two image clips in Fig. 4 (b) and (c) showing overall segmentation result and ground-truth, it is obvious that the overall segmentation result is satisfactory. Particularly the segmentation of cell boundaries in conglomerating sets of cells is of high quality. In outer

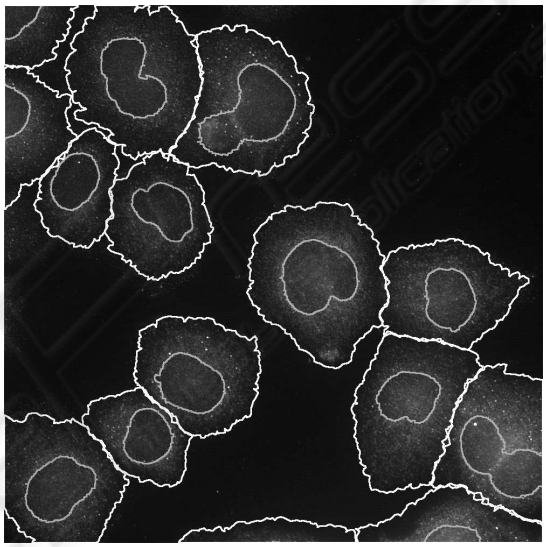

Figure 7: Cell segmentation result on complete image, final contours are shown in white, initial nuclei contours in gray.

sections of the cells sometimes fractions of the cell area are still missing. However, as the figures below indicate the missing sections only marginally degrade the quality of the results. This is due to the fact that for our application the main focus is the correct assignment of PBs and SGs to cells, and the distribution of their numbers and localization with respect to the cells and their nuclei.

The main idea of our 3-level approach is to iteratively improve segmentation results. During level one large parts of the cell are still missing, while in latter levels almost the complete cell area is included in the segmentation result. This is exemplary shown in Figure 6 for a clip of one image which also demonstrates the incremental improvement of cell segmentation, which cannot be achieved in one single snake segmentation run. Fig. 7 shows final cell contours as extracted by our new approach for a complete image of the test set emphasizing again the high performance of the algorithm in adequately separating conglomerating cells.

Cell segmentation can be regarded a classification task on the pixel level. For optimal results each pixel of a labeled ground-truth cell should be segmented by the algorithm and correctly classified into the correct cell class. These pixels correctly classified as cell pixels are the true positives (TP), while pixels incorrectly classified as cell pixels are false positives (FP). Pixels incorrectly classified as background or belonging to other cells are false negatives (FN). Based on this interpretation for each ground-truth cell, precision and recall can be calculated. The recall $TP/(TP+FN)$ is defined as the ratio of ground-truth pixels that were actually correctly detected by the segmentation algorithm, while the precision $TP/(TP+FP)$ gives the ratio of detected cell pixels that are actually lying inside ground-truth cells. In Figures 8 and 9 box-plots for the recall and precision achieved are presented. For each of the three segmentation levels the values are shown, in each case averaged over all 77 cells.

Considering the recall its median steadily increases from 0.66 after the first segmentation level to 0.79 and finally 0.91 after the last level. This is due to the fact that beginning with the initial nucleus region in each level the algorithm segments larger fractions of the cells.

For the precision the tendency is just conversely. Since the initial cell regions are derived from the nuclei segmented, the contours from the first level predominately lie completely within the surrounding cells, i.e. very few false negatives appear in the segmentation. With evolving snake contours the cell area grows, and consequently the chance to include pixels into the snake region that actually belong to the background or other cells increases. The precision decreases from an initial median of 0.99 to a final value of 0.92. Note that for more than 75% of the cells the value still exceeds 0.84.

In both plots outliers with recall and precision values close to zero can be observed. On the one hand these result from very small cells that are enclosed into the area of significantly larger cells in their neighborhood during segmentation resulting in a significant amount of false positives and small precision, respectively. One the other hand the outlier cell with very low recall values relates to a ground-truth cell located near the image boundary where only small fractions of the cell nucleus are visible. Consequently the initial snake contains only very few polygon points and rapidly collapses rather than to segment the cell. Altogether precision and recall indicate that the segmentation misses some fractions of several cells, but barely includes additional non-cell pixels.

From the biological point of view besides the actual automatic detection of PBs and SGs one very valuable information is the distribution of the particles with regard to the cells. In detail, different biological implications result if the particles are equally spread over all cells of a sample or quite inhomogeneously distributed in the cell population. Therefore we assess the assignment of the PBs and SGs to the different cells compared to ground-truth cell segmentation. In Figures 10 and 11 the corresponding scatter plots are shown.

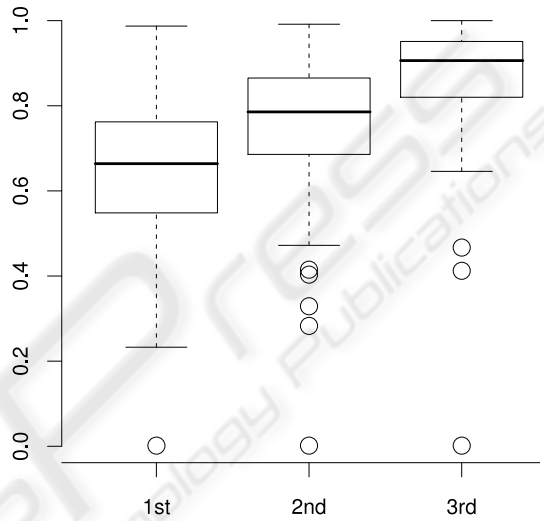

Figure 8: Average recall values for all 77 cells.

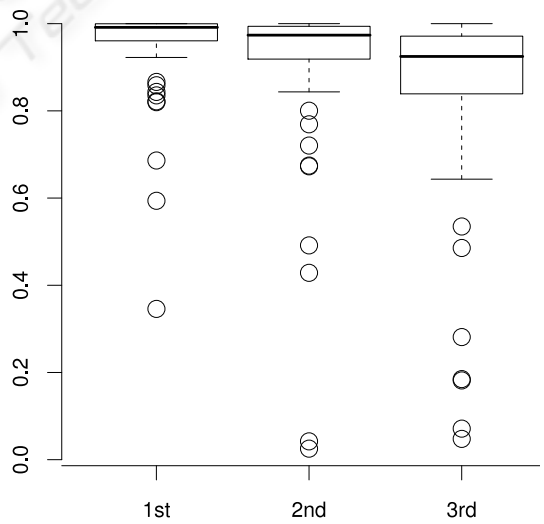

Figure 9: Average precision values for all 77 cells.

On the abscissa of each plot the number of particles, either PBs or SGs, in a ground-truth cell is shown, on the ordinate the automatically detected number of PBs or SGs in the corresponding cell segmented via snakes is outlined. In case of optimal particle assignment from correctly segmented cell areas

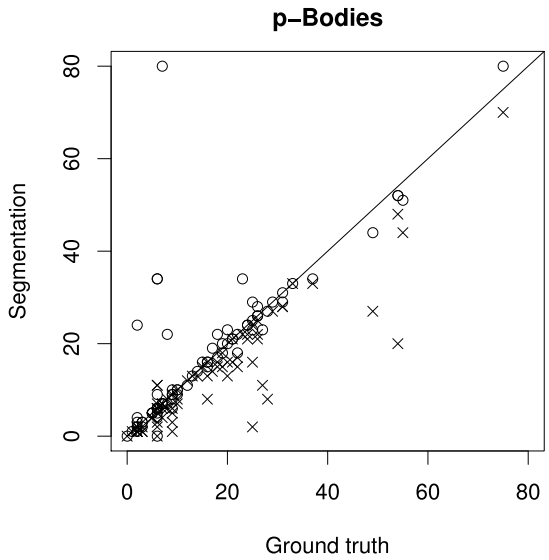

Figure 10: Number of cooccurring PBs in ground-truth and segmented cells after the first segmentation level (cross) and in the final result (circle).

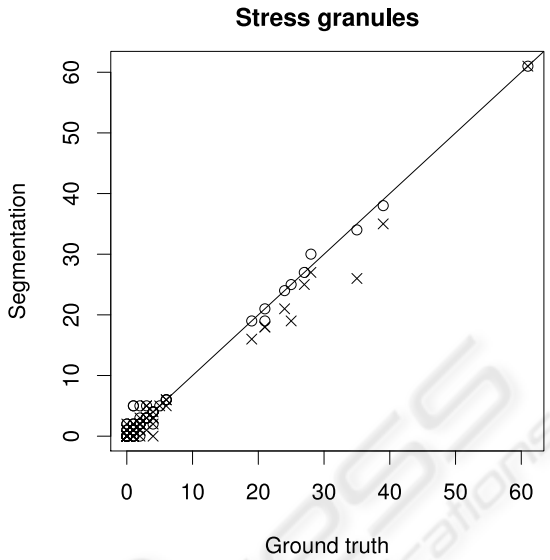

Figure 11: Number of cooccurring SGs in ground-truth and segmented cells after the first segmentation level (cross) and in the final result (circle).

the plots should show a perfect bisecting line. In both plots the results after the first iteration are shown as crosses, while the final results are marked by circles. Note that in the setup of the biological experiment the number of SGs in the images is in general significantly smaller than the number of PBs. Nevertheless in both plots it is clearly visible that the cooccurence increases. Regarding SGs the Spearman rank correlation coefficient slightly increases from 0.852 to 0.888.

Also for PBs the majority of data points moves towards the bisecting line. The correlation value decreases from initially 0.891 to 0.853 and finally 0.832. The main reason for this are two collapse events during segmentation leading to wrong cell correspondences. In both cases at the beginning a set of three ground-truth cells is corresponding to exactly three snake contours. In the course of the segmentation, however, one of the snakes collapses and the cell is included in the area of a neighboring snake (cf. Fig. 12). Consequently a single segmented cell corresponds to two ground-truth cells, whereas only one of them is the correct one while the second ground-truth cell gets assigned many false positive detection results. In the plot in Fig. 10 the outlier point in the top left corner of the plot is caused by one of these events.

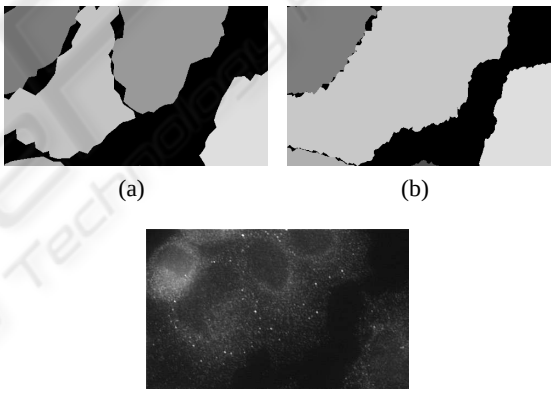

Figure 12: Example for segmentation failure. While in level 2 (a) three snake regions model the ground-truth cells, in level 3 (b) one snake disappears allowing one of the remaining two to wrongly occupy its region as well. Note that the cells are hard to separate even manually (c).

6 CONCLUSIONS

We proposed two techniques for automatic analysis of fluorescence microscopy images: one algorithm to segment the areas of cells, and a second one for the detection of sub-cellular particles, namely PBs and SGs. For particle detection we extend an approach based on correlated wavelet coefficients from the a trous wavelet transform. To accommodate particles of varying size we introduce a set of scale intervals and resolve ambiguities in the resulting particle hypotheses by adapting the concept of meaningful events. Secondly, for the segmentation of cell areas composed of nested rings of decreasing intensities we expand a coupled active contour model into a cascaded segmentation technique. The core idea of this technique is to incrementally incorporate the intensity rings into the segmentation result, starting with the nucleus of

each cell as initialization. Our algorithms are evaluated on a set of 5 images with cells of a human hepatoma cell line, each composed of three channels labeling nuclei, SGs and PBs, respectively. The results clearly show the benefits of the cascaded approach as the overall segmentation quality is high. This is true as well for precision and recall of cell areas as for the assignment of particles to their corresponding cells. Future work will include improvements of nucleus segmentation to avoid or correct fusion of neighboring nuclei. Furthermore, data-depended adaption of the number of levels used in the cascaded approach with an appropriate stopping criterium will be scrutinized.

REFERENCES

Bolte, S. and Cordelieres, F. P. (2006). A guided tour into subcellular colocalization analysis in light microscopy. *Journal of Microscopy*, 224(3):213–232.

Chan, T. and Vese, L. (2001). Active contours without edges. *IEEE Transactions on image processing*, 10(2):266–277.

Desolneux, A., Moisan, L., and Morel, J.-M. (2003). A grouping principle and four applications. *IEEE Trans. PAMI*, 25(4):508–513.

Dufour, A., Meas-Yedid, V., Grassart, A., and Olivo-Marin, J. (2008). Automated quantification of cell endocytosis using active contours and wavelets. In *Pattern Recognition, 2008. ICPR 2008. 19th International Conference on Pattern Recognition*.

Dufour, A., Shinin, V., Tajbakhsh, S., Guillen-Aghion, N., Olivo-Marin, J., and Zimmer, C. (2005). Segmenting and tracking fluorescent cells in dynamic 3-D microscopy with coupled active surfaces. *IEEE Transactions on Image Processing*, 14(9):1396–1410.

Dzyubachyk, O., Niessen, W., and Meijering, E. (2007). A variational model for level-set based cell tracking in time-lapse fluorescence microscopy images. In *IEEE International Symposium on Biomedical Imaging*. IEEE, Piscataway.

Dzyubachyk, O., Niessen, W., and Meijering, E. (2008). Advanced level-set based multiple-cell segmentation and tracking in time-lapse fluorescence microscopy images. In *IEEE International Symposium on Biomedical Imaging*. IEEE, Piscataway.

Eulalio, A., Behm-Ansmant, I., and Izaurralde, E. (2007). P bodies: at the crossroads of post-transcriptional pathways. *Nature Reviews Molecular Cell Biology*, 8:9–22.

Figueiredo, M. A. T. and Nowak, R. D. (2001). Wavelet-based image estimation: an empirical bayes approach using jeffrey's noninformative prior. *IEEE Trans. IP*, 10(9):1322–1331.

Genovesio, A., Liedl, T., Emiliani, V., Parak, W., Coppey-Moisan, M., and Olivo-Marin, J. (2006). Multiple Particle Tracking in 3-D+ Microscopy: Method and Application to the Tracking of Endocytosed Quantum Dots. *IEEE Transactions on Image Processing*, 15(5).

Greß, O., Möller, B., Stöhr, N., Hüttelmaier, S., and Posch, S. (2010). Scale-adaptive wavelet-based particle detection in microscopy images. In *Proceedings of the Workshop Bildverarbeitung für die Medizin (BVM)*. Springer. accepted for publication.

Kass, M., Witkin, A. P., and Terzopoulos, D. (1988). Snakes: Active contour models. *International Journal of Computer Vision*, 1(4):321–331.

Olivo-Marin, J. (2002). Extraction of spots in biological images using multiscale products. *Pattern Recognition*, 35(9):1989–1996.

Smal, I., Niessen, W., and Meijering, E. (2008). A new detection scheme for multiple object tracking in fluorescence microscopy by joint probabilistic data association filtering. In *5th IEEE International Symposium on Biomedical Imaging: From Nano to Macro, 2008. ISBI 2008*, pages 264–267.

Xavier, J., Schnell, A., Wuertz, S., Palmer, R., White, D., and Almeida, J. (2001). Objective threshold selection procedure (OTS) for segmentation of scanning laser confocal microscope images. *Journal of microbiological methods*, 47(2):169.

Yamasaki, S. and Anderson, P. (2008). Reprogramming mRNA translation during stress. *Curr. Opin. Cell Biol.*, 20:222–226.

Zimmer, C. and Olivo-Marin, J. (2005). Coupled parametric active contours. *IEEE transactions on pattern analysis and machine intelligence*, 27(11):1838–1842.